# Supporting Information

## The lattice Strain Dominated Catalytic Activity in Single-Metal Nanosheet

Meng Wang,†[a] Qintao Sun,†[a] Zhenglong Fan,†*[a] Wenxiang Zhu,[a] Fan Liao,[a] Jie Wu,[a] Yunjie Zhou,[a] Hao Yang,[a] Hui Huang,[a] Mengjie Ma,[a] Tao Cheng,*[a] Qi Shao,*[b] Mingwang Shao,*[a] Zhenhui Kang*[a,c]

E-mail: zlfan@suda.edu.cn; tcheng@suda.edu.cn; qshao@suda.edu.cn; mwshao@suda.edu.cn;

zhkang@suda.edu.cn

### Experimental Section

**1.1 Chemicals.** Iridium (III) chloride ($IrCl_3$) were bought from Alfa Aesar Co. Commercial Pt/C (platinum, nominally 20 wt% on carbon black) catalyst was supported by Alfa Aesar Co. Potassium hydroxide (KOH) was supported by Sinopharm Chemical Reagent Co. Hydrochloric acid (HCl) was obtained from Chinasun Specialty Products Co. Nafion solution (5 wt%) was supported by Sigma-Alddrich Co. Isopropanol was bought from Sinopharm Chemical Reagent Co.

**1.2 Synthesis of 3R-$IrO_2$ and Rutile-$IrO_2$.** The 3R-$IrO_2$ was obtained by a molten alkali-assisted synthesis method in a home-made reactor. In brief, 300 mg $IrCl_3$ and 10 g KOH were added in a reactor. The above mixture was heated in a microwave oven for 30 mins together with continuously grinding, and then naturally cooled to room temperature. The sample was cleaned by 1 M HCl and double-distilled water for several times respectively, dried by lyophilization to obtain final product of 3R-$IrO_2$. Rutile-$IrO_2$ was obtained by directly annealing 3R-$IrO_2$ at 900 °C for 2 h in air atmosphere.

**1.3 Synthesis of Ir-PFNSs and Metallic Ir.** The porous flexible iridium nanosheets (Ir-PFNSs) were obtained by directly annealing 3R-$IrO_2$ nanosheets at different temperatures in hydrogen atmosphere (5 wt% $H_2$ and 95 wt% Ar) for 2 h. The metallic Ir were obtained under same condition, where Rutile-$IrO_2$ was used as precursors to replace 3R-$IrO_2$.

**1.4 Structure Characterization of 3R-$IrO_2$.** It is necessary to discuss the preparation and crystal structure of 3R-$IrO_2$ precursor. As depicted in Fig. S4, the 3R-$IrO_2$ was obtained by a molten alkali-assisted synthesis method in a home-made reactor,[1] where iridium chloride ($IrCl_3$) and potassium hydroxide (KOH) were selected as raw materials. As shown in Fig. S5a, the 3R-$IrO_2$ shows a dark blue color, which is different from black Rutile-$IrO_2$ (Fig. S5b). The X-ray powder diffraction (XRD) was applied to reveal the crystal structure of 3R-$IrO_2$ and corresponding crystal parameters were determined to be $a = b = 3.158$ Å, $c = 13.617$ Å with space group of R-3m (166) (Fig. 1b). The thickness of 3R-$IrO_2$ is about 1.5 nm, revealed by AFM image (Fig. S5c). The aberration-corrected dark-field scanning transmission electron microscopy (STEM-ADF) image of 3R-$IrO_2$ nanosheet was shown in Fig. S6, which may clearly observe its hexagonal lattice. The distance between two adjacent atoms was determined to be 3.11 Å by STEM-ADF image, which is almost same with XRD results. Selected area electron diffraction (SAED) of 3R-$IrO_2$ shows a hexagonal pattern, attributing to its 3R phase structure (Fig. S5g). The elemental analysis results further indicate the atomic ratio of Ir and O in 3R-$IrO_2$ is about 1: 2 (Fig. S5i). XPS was considered as an effective characterization method to reveal electronic state of 3R-$IrO_2$. As shown in Fig. S7a, the Ir 4f binding energies of 3R-$IrO_2$ have no significant difference to those of Rutile-$IrO_2$,[2] indicating the valence state of Ir ion in 3R-$IrO_2$ is closed to +4. Moreover, the Ir-O bond may be clearly observed in both 3R-$IrO_2$ and Rutile-$IrO_2$ (Fig. S7b). All these results conclude that a metastable 3R phase $IrO_2$ with the space group of No. 166 (R-3m) has been successfully prepared (Table S1) and the corresponding structure of 3R-$IrO_2$ is shown in Fig. S8.

**1.5 Williamson-Hall equation derivation[3].**

The total broadening equation:

$$\beta = \beta_D + \beta_\varepsilon \quad (1)$$

The Debye-Scherrer's equation:

$$D = \frac{k\lambda}{\beta_D cos\theta} \quad (2)$$

Can be converted into:

$$\beta_D = \frac{k\lambda}{Dcos\theta} \quad (3)$$

The strain equation:

$$\beta_\varepsilon = 4\varepsilon tan\theta \quad (4)$$

Bring equation (3) and equation (4) into equation (1):

$$\beta = \frac{k\lambda}{Dcos\theta} + 4\varepsilon tan\theta \quad (5)$$

Can be converted into:

$$\beta cos\theta = \frac{k\lambda}{D} + 4\varepsilon sin\theta \quad (6)$$

β is the total broadening; $\beta_D$ is the broadening due to crystallites size; $\beta_\varepsilon$ is the broadening due to strain. D is the crystallites size; θ is the Bragg angle; K is shape factor, λ= 0.15046 nm is the wavelength of Cu Kα. ε is the strain. The equation (6) is Williamson-Hall equation, which can be seen as an equation y= kx + b, βcosθ is Y axis, 4sinθ is X axis and the slope is ε.

**1.6 Electrochemical Measurements.** CHI 760D electrochemical workstation with a standard three-electrode system was used to conduct HER experiments. A carbon rob and a saturated calomel electrode (SCE) were selected as counter electrode and the reference electrode, respectively. A modified glassy carbon electrode (GCE) with diameter of 3 mm was chosen for working electrode. The preparation for catalyst was displayed as follow: 2 mg catalyst (0.4 mg Ir-PFNSs-300, 1.6 mg carbon black) was added into the mixed solution (450 $\mu$L isopropanol and 50 $\mu$L 0.5 wt% Nafion solution) and ultrasonicated to obtain the homogenous ink. And then 4 $\mu$L above dispersion was dropped on the surface of GCE and dried naturally for HER measurements. HER performance was analyzed by linear sweep voltammetry (LSV) with the scan rate of 5 mV $s^{-1}$ and 95% iR-correction in $H_2$-saturated 0.5 M $H_2SO_4$. HER stability was measured by chronopotentiometry under a constant current density of -10 mA $cm_{geo}^{-2}$ in $H_2$-saturated 0.5 M $H_2SO_4$, The working electrode was prepared as follow: 2 mg catalyst (Ir-PFNSs-300, Pt/C and Ir-300) was added into the mixed solution (450 μL isopropanol and 50 μL, 0.5 wt% Nafion solution) and ultrasonicated to form the homogenous ink. 50 μL above dispersion was dropped on the surface of carbon paper (0.5 cm × 1 cm) and dried naturally for stability test.

ECSA of iridium or iridium oxides was determined by mercury (Hg) underpotential deposition method, the detailed measurement procedures are displayed as follow: 2 mg catalyst (Ir-PFNSs-300, Ir-300 and Pt/C) was added into mixed solution (3.6 mL isopropanol and 400 $\mu$L 0.5 wt % Nafion solution) and ultrasonicated to from homogenous catalysts ink. Then 6 $\mu$L above dispersion was dropped on the surface of GCE and dried naturally for measurement. Cyclic voltammograms (CVs) with scan rate of 100 mV $s^{-1}$ and a potential range of 0.145-0.645 V (vs. RHE) were performed in 0.1 M $HClO_4$ solution containing 1 mM mercury nitrate. the

ECSA of Pt/C was determined from hydrogen under potential deposition ($ECSA_{Hupd}$) by performing CV in $N_2$-saturated 0.5 M $H_2SO_4$ with a scan rate of 50 mV $s^{-1}$ and ranging from 0 to 1.345 V (vs. RHE). The Coulombic charge of hydrogen is 210 $\mu$C $cm_{Pt}^{-2}$, which may go back to Li's report.[4] The corresponding equations of Hg underpotential deposition method are shown as follow:[1,5]

$$ECSA = \frac{Q}{C} \quad (7)$$

$$Q = \frac{S_{peak}}{v} \quad (8)$$

C is Coulombic charge of 138.6 $\mu$C $cm_{Ir}^{-2}$. Speak is the integral area of adsorbed mercury in the CV curve and v is the scan rate of 100 mV $s^{-1}$.

**1.7 DFT Calculations.** The *ab* initio quantum mechanical (QM) calculations are performed using Vienna Ab initio Simulation Package (VASP) at a version of 5.4.4 with the projector augmented wave (PAW) method and a plane wave basis set. The method is density functional theory (DFT) with generalized gradient approximations (GGA) of Perdew-Burke-Ernzerhof (PBE) functional.[6] A dispersion correction, DFT-D3 method with Becke-Jonson damping,[7] was included in the calculations. The energy cut-off is set to 400 eV. Larger energy cut-off does not produce more accurate prediction basing on our benchmark calculation. Reciprocal space was sampled by Γ-centered Monkhorst-Pack scheme with a grid of 3×3×1. Finer K spacing does not produce more accurate prediction basin on our benchmark calculation. Spin polarization does not have an appreciable effect on the overall energies and is not included in the calculations to reduce computational demands. The partial occupancies for each orbital are set with the first order Methfessel-Paxton scheme in the smearing width of 0.2 eV. The dipole moment corrections for the total energy are considered in the direction normal to the surface. The self-consistent electronic step is considered converged when the change of total energy and eigenvalues change between two steps are both smaller than $1e^{-5}$ eV. The implicit solvation model of VASP sol is employed to describe the effect of electrostatics, cavitation, and dispersion on the interaction between a solute and solvent.[8,9] The relative permittivity of the solvent is 78.4, and the Debye screening length is 3.0 Å. The number of electrons in the simulations was tuned to match the target chemical potential of electron.

**1.8 Geometry Optimization.** Structural optimization was carried out for each structure. A conjugate-gradient algorithm is used to relax the ions in energy minimization. The minimization was considered converged when all the atomic force was are smaller than 0.02 eV/Å, where convergence to an energy minimum was confirmed in all cases with frequency calculations to verify that all imaginary frequencies were eliminated.

**1.9 Entropy Correction.** The frequencies and normal modes are determined from the Hessian matrix. To calculate the Hessian matrix, finite differences are used. Each ion is displaced ±0.04 A in the direction of each cartesian coordinate, and from the forces the Hessian matrix is determined. Only the adsorbed species are populated in the frequency calculation, while the slab atoms were kept fixed. The temperature is 298 K, and the pressure is 1 bar.

Free energies for all structures were computed using standard statistical mechanics formula that accounts for translational, rotational, vibrational, and electronic degrees of freedom.[10] Translational and rotational contributions to the free energy were omitted for all surface adsorbed species. The estimation of the thermodynamics is briefly summarized as follows.

The partition function under the harmonic oscillator approximation is as follows:

$$q_{vib} = \prod_i \frac{e^{-hv_i/2kT}}{1 - e^{-hv_i/kT}} \quad (9)$$

where k is a force constant, $v$ is the vibrational frequency, after substituting the partition function $q_{vib}$, the internal energy correction is as follows:

$$U_{vib}(T) = R\sum_i \left(\frac{hv_i}{k}\right)\left(\frac{1}{2} + \frac{e^{-\frac{hv_i}{kT}}}{1 - e^{-\frac{hv_i}{kT}}}\right) \quad (10)$$

The first term is the contribution of zero-point energy (ZPE), and the second term is the contribution of internal energy correction from 0 K to 298K.

The correction of entropy (S) is as follows:

$$S_{vib}(T) = R\sum_i \left\{\frac{hv_i}{kT}\frac{e^{-\frac{hv_i}{kT}}}{1 - e^{-\frac{hv_i}{kT}}} - ln\left[1 - e^{-\frac{hv_i}{kT}}\right]\right\} \quad (11)$$

Here, the first term exactly cancels with the second term of the internal energy shown above. Therefore, only the second term of the entropy needs to be corrected.

For adsorbed species, the six degrees of freedom of the translation and rotation are frustrated and considered vibration. Such approximation fails when the vibration is extremely low that has a significant contribution to the correction. To avoid such overestimation, the contribution of frequencies below 50 $cm^{-1}$ are all considered as 50 $cm^{-1}$.

Zero-point energy (ZPE) in thermo energy correction is as follows:

$$\varepsilon_{ZPE} = \frac{hv}{2} \quad (12)$$

The Gibbs free energy G can be derived as follows:

$$G = E_{ZPE} + E + k_B T - TS \quad (13)$$

The above correction is obtained by using VASPKIT code for a post-processing of the VASP calculated data.[2]

**1.10 Details of the Simulated Models.** Different compressive strain models: We achieved the compressive strain by shrinking the a-axis and b-axis of the super cell, and the shrinkage of the a-axis and b-axis was the same.

$H_3O^+$ modeling details: The initial state of $H_3O^+$ model is to place a $H_3O^+$ ion on the substrate with hydrogen adsorption, where hydrogen atoms are adsorbed on all face-centered cubic (fcc) hollow sites. In order to stabilize $H_3O^+$, we put three $H_2O$ molecules around the $H_3O^+$ (Fig. S18c and S18g). The final state model is built based on the initial state model. The two H atoms adsorbed on the fcc hollow site combine to form $H_2$, while the H ion of $H_3O^+$ is adsorbed on the substrate. Meanwhile, a $H_2O$ adsorbed on the substrate, and hydrogen bonds are formed between $H_2O$ and $H_2O$ (Fig. S18d and S18h). After testing, such a final state structure is the most stable existence.

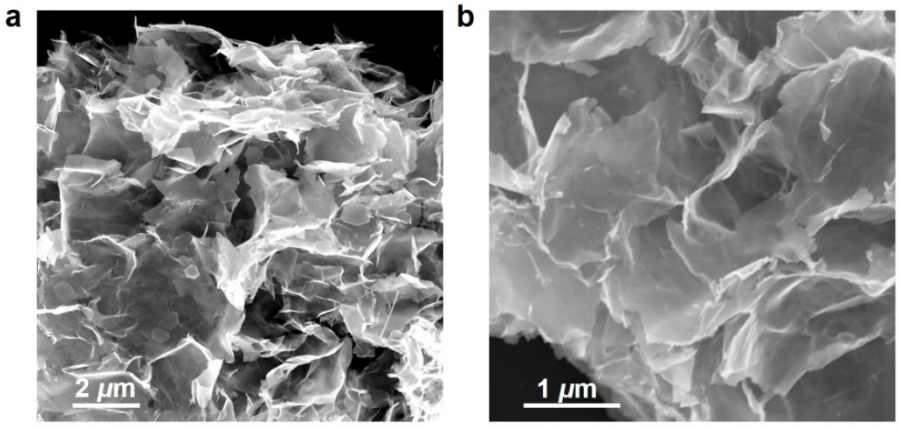


**Figure S1.** SEM images of (a) Ir-PFNSs and (b) 3R-$IrO_2$, representing their ultrathin flexible nanosheets morphology.

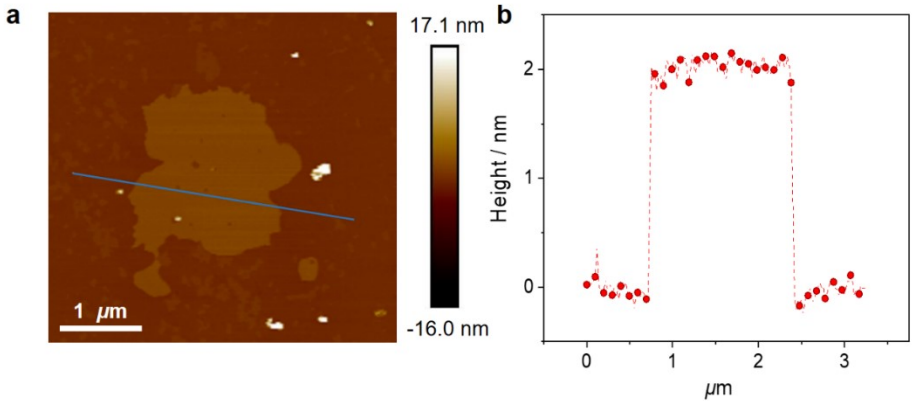


**Figure S2.** AFM image and corresponding height profile of Ir-PFNSs, where the height of Ir-PFNSs was determined to be 2.1 nm.

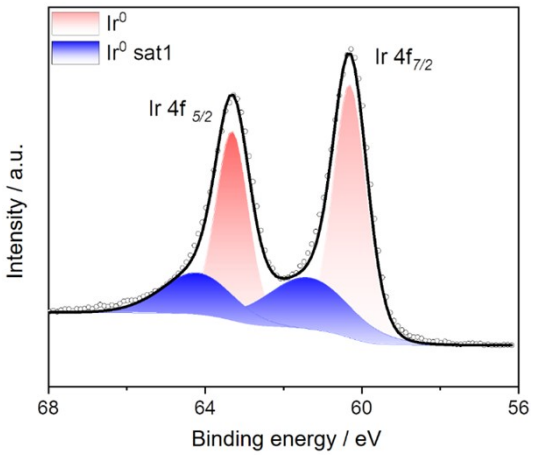


**Figure S3.** XPS spectrum of Ir 4f peaks for Ir-PFNSs-300. The peaks at 60.9 eV and 63.9 eV may be completely attributed to metallic Ir for the $4f_{7/2}$ and $4f_{5/2}$, respectively.

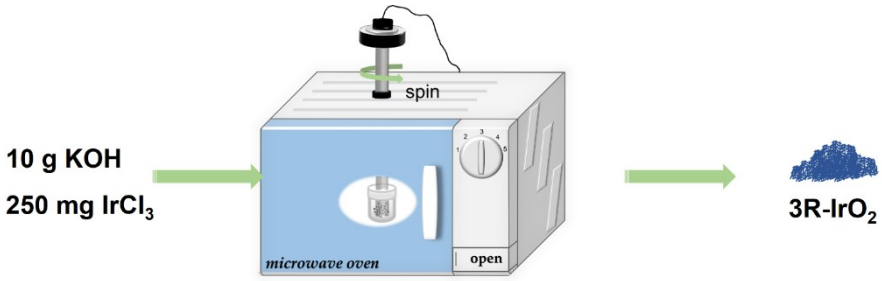


**Figure S4.** Schematic synthesis of molten alkali-assisted synthesis method to obtain 3R-$IrO_2$.

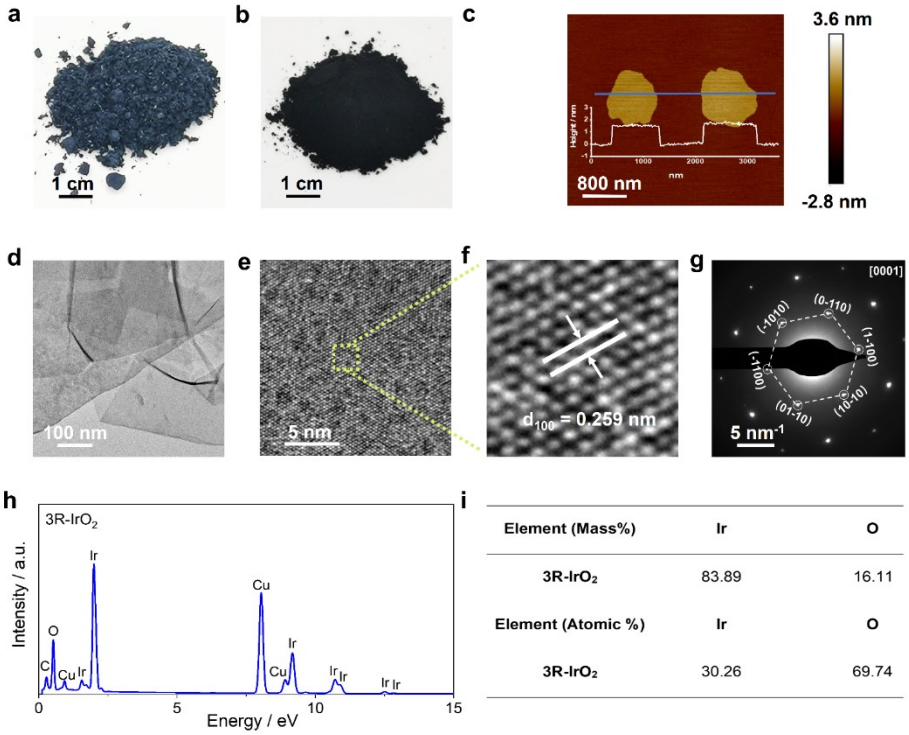


| Element (Mass%) | Ir | O |
|---|---|---|
| 3R-IrO$_2$ | 83.89 | 16.11 |
| **Element (Atomic %)** | **Ir** | **O** |
| 3R-IrO$_2$ | 30.26 | 69.74 |

**Figure S5.** Structural characterization of 3R-$IrO_2$. (a) The digital image of 3R-$IrO_2$ powder. (b) The digital image of Rutile-$IrO_2$ powder. (c) AFM image and corresponding height profile of 3R-$IrO_2$. (d-f) TEM and HRTEM images of 3R-$IrO_2$. (g) The SAED pattern of 3R-$IrO_2$. (h) EDX analysis of 3R-$IrO_2$. (i) The table of the mass and atomic ratios for Ir and O in 3R-$IrO_2$ by elemental analysis method (elementar EL III).

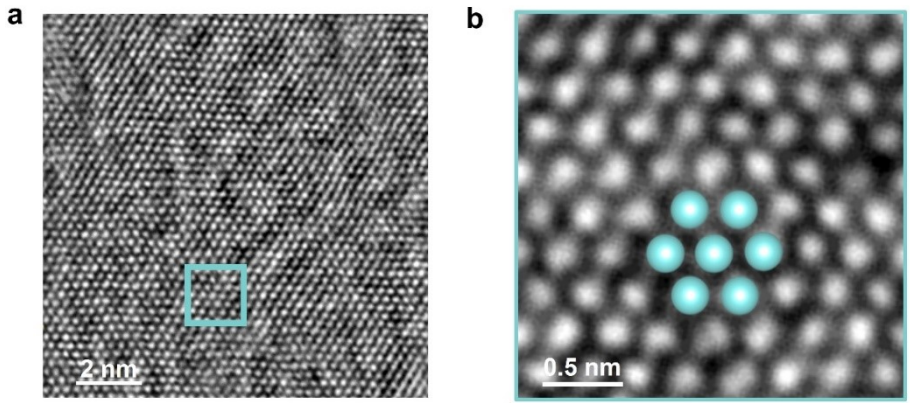


**Figure S6.** STEM-ADF image of 3R-$IrO_2$. (a) STEM-ADF images of 3R-$IrO_2$ and (b) its partial enlargement, clearly observing its hexagonal lattice.

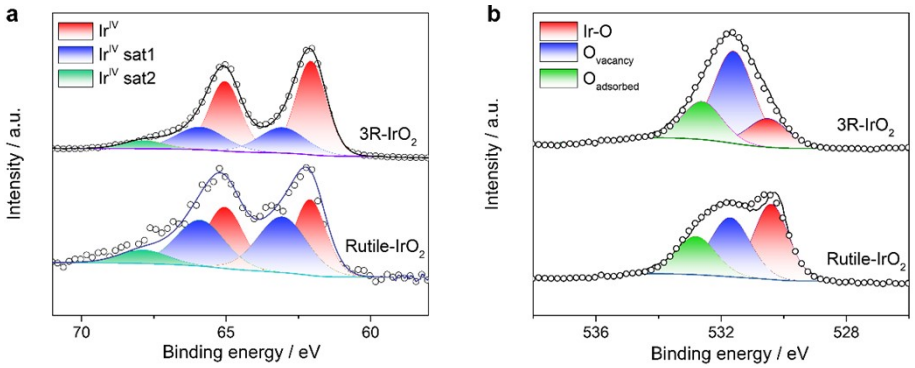


**Figure S7.** The measurements of XPS for 3R-$IrO_2$ and Rutile-$IrO_2$. (a) XPS spectra of Ir 4f peaks for 3R-$IrO_2$ and Rutile-$IrO_2$. (b) XPS spectra of O 1s peaks for 3R-$IrO_2$ and Rutile-$IrO_2$.

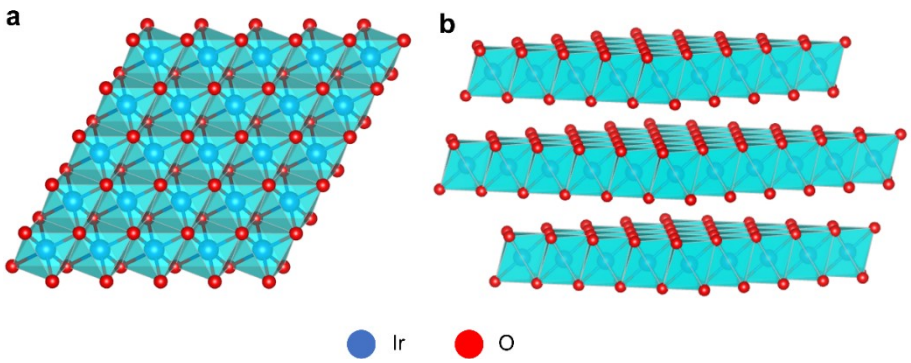


**Figure S8.** (a, b) The structure schemes of 3R-$IrO_2$ from different directions.

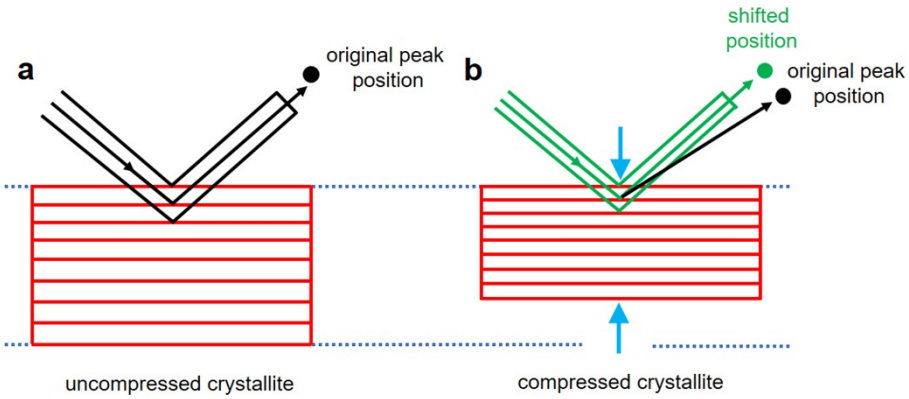


**Figure S9.** Schematic representation of the shift of XRD peaks for (a) uncompressed and (b) compressed crystallites.

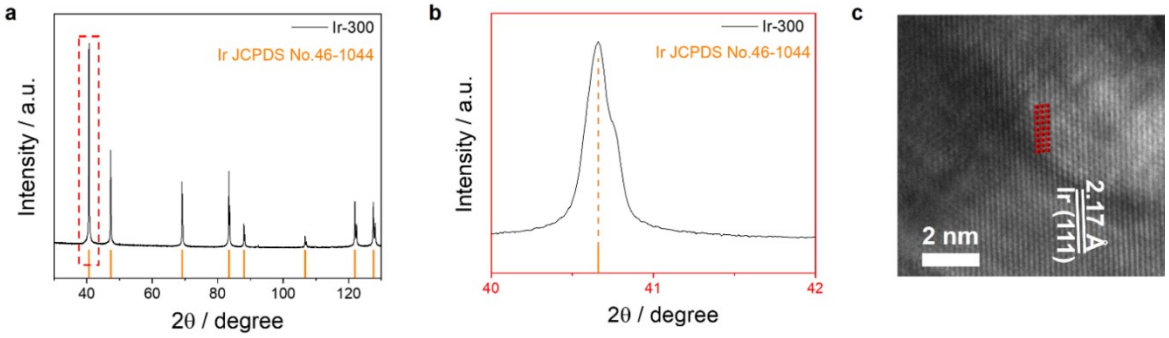


**Figure S10.** XRD pattern and HRTEM image of Ir-300. (a) XRD pattern of Ir-300 and (b) its partial enlargement, where the annealing temperature is 300 °C. (c) The HRTEM image of Ir-300.

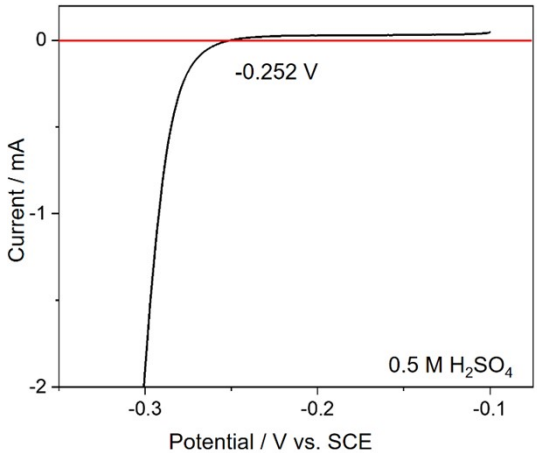


**Figure S11.** Calibration of the saturated calomel electrode (SCE). Calibration of the saturated calomel electrode (SCE) electrode in 0.5 M $H_2SO_4$ electrolytes bubbled with pure hydrogen gas at room temperature. Scan rate: 5 mV $s^{-1}$.

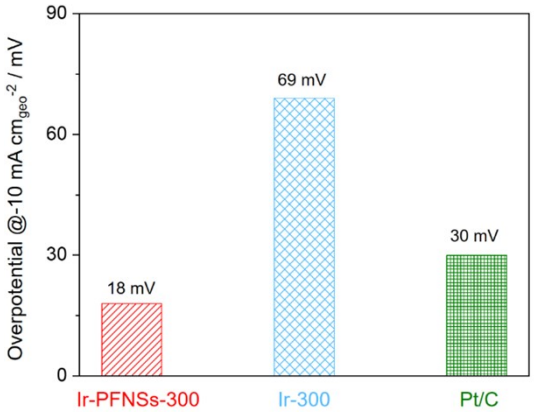


**Figure S12.** The overpotentials of Ir-PFNSs-300, Ir-300 and Pt/C at the current density of -10 mA $cm_{geo}^{-2}$.

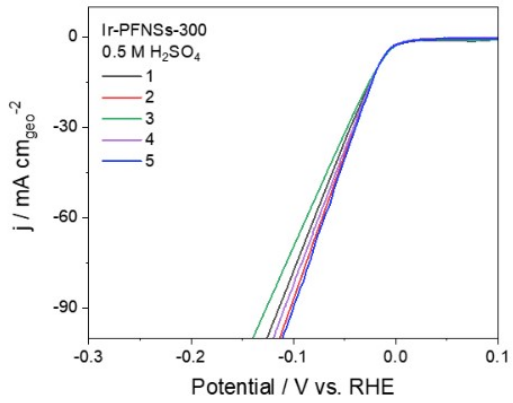


**Fig. S13.** Reproducibility of HER performance measured by 5 different electrodes of Ir-PFNSs-300 in 0.5 M $H_2SO_4$.

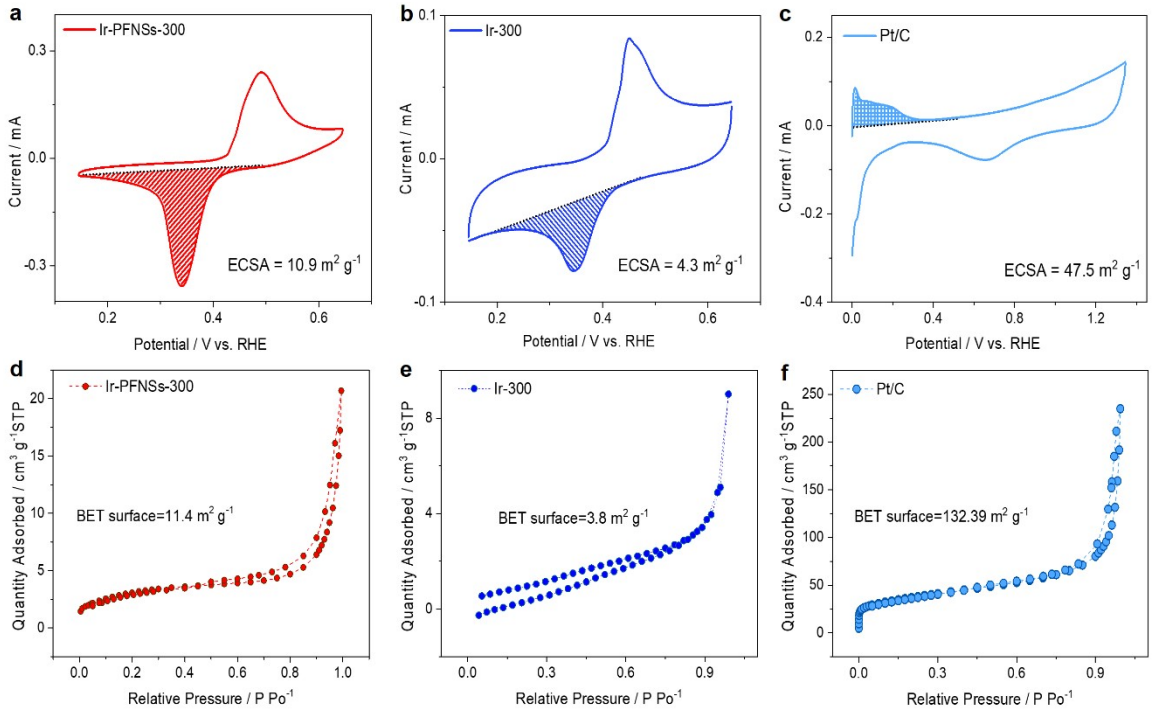


**Figure S14.** The ECSA and BET curves of Ir-PFNSs-300, Ir-300 and Pt/C. (a) CVs of Ir-PFNSs-300, where the ECSA of Ir-PFNSs-300 was calculated to be 10.9 $m^2 g^{-1}$. (b) CVs of Ir-300, where the ECSA of Ir-300 was calculated to be 4.3 $m^2 g^{-1}$. (c) CVs of Pt/C, where the ECSA of Pt/C was calculated to be 47.5 $m^2 g^{-1}$. (d-f) BET surface area measurements for Ir-PFNSs-300, Ir-300 and Pt/C, respectively.

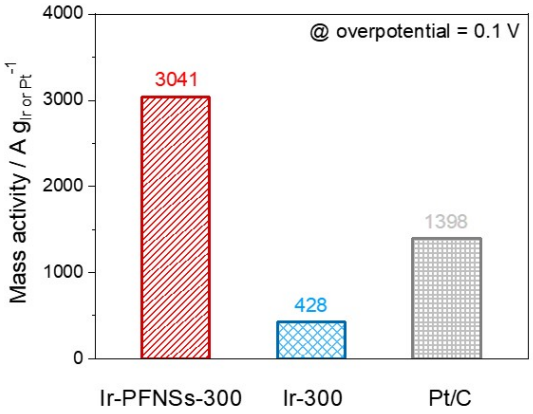


**Figure S15.** Mass activities of Ir-PFNSs-300, Ir-300 and Pt/C at the overpotential of 0.1 V.

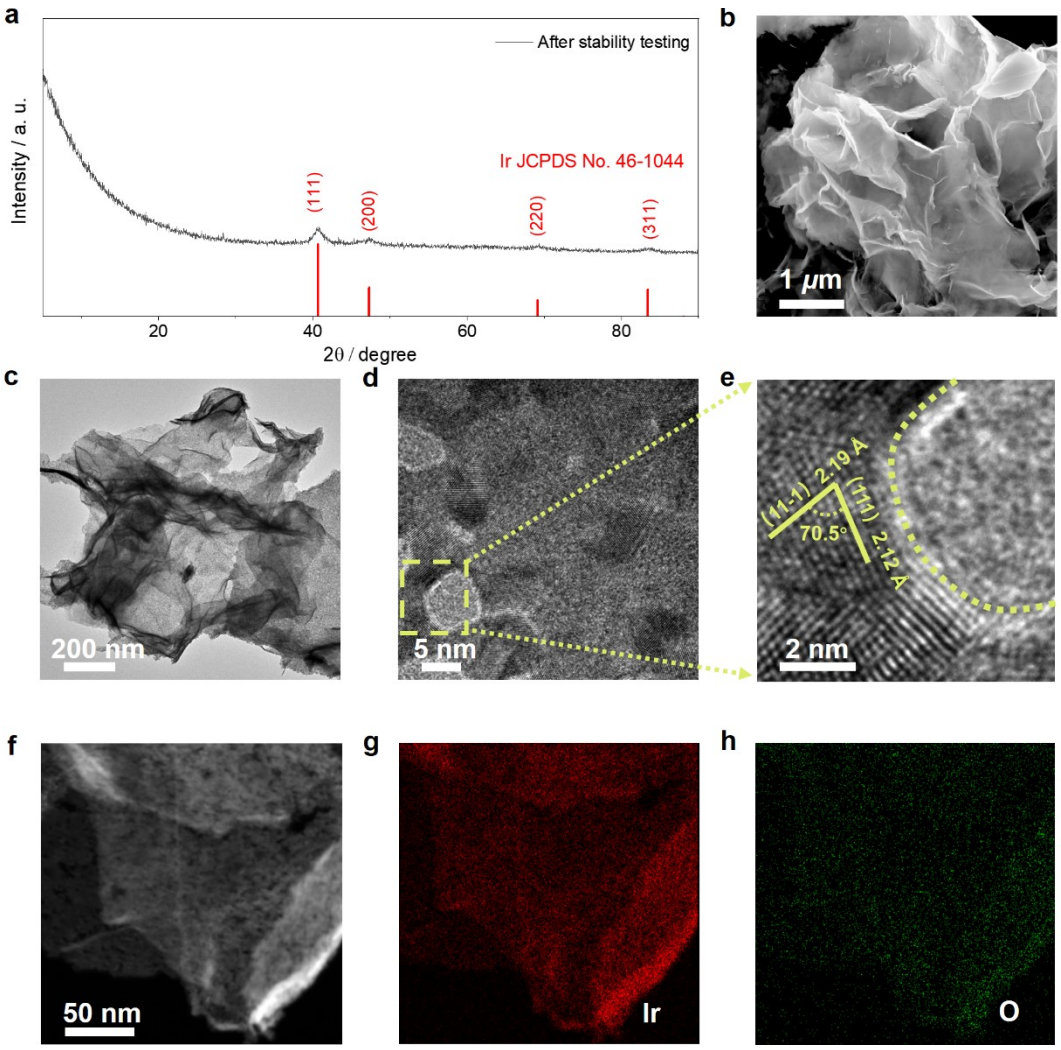


**Figure S16.** XRD patterns, SEM image, TEM image, HRTEM image and TEM-EDX mapping of Ir-PFNSs-300 after stability test. (a) XRD pattern, (b) SEM, (c) TEM, (d, e) HRTEM and (f-h) EDX-mapping images of Ir-PFNSs-300 after long-term stability test.

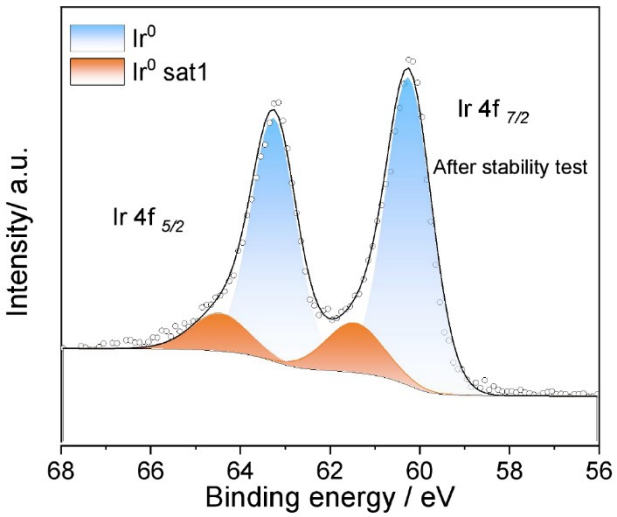


**Figure S17.** XPS spectrum of Ir 4f peaks for Ir-PFNSs-300 after long-term HER stability test, where the peaks at 60.9 eV and 63.9 eV may be completely attributed to metallic Ir for the $4f_{7/2}$ and $4f_{5/2}$, respectively.

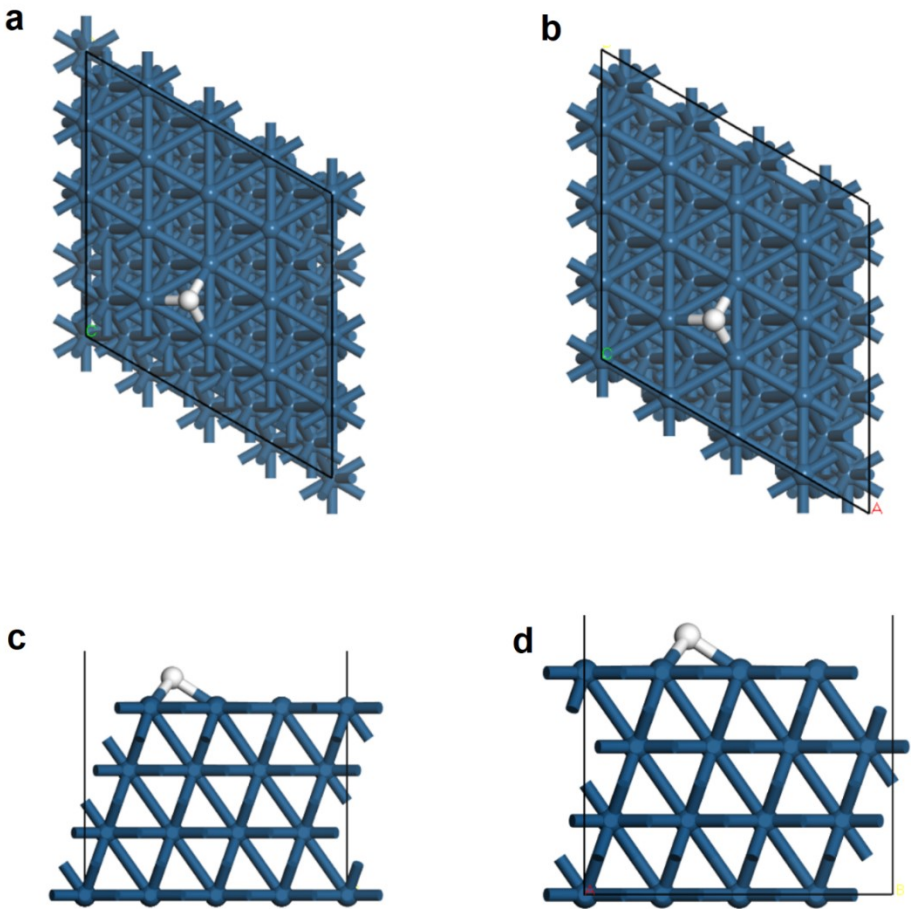


**Figure S18.** The atomic model of Ir-PFNSs for DFT calculations. (a) and (b) are top views of the H adsorption model with compressive strain of 0 and -1.26%, respectively. (c) and (d) are side views of the H adsorption model with compressive strain of 0 and -1.26%, respectively. Color code: Iridium, blue; hydrogen, white.

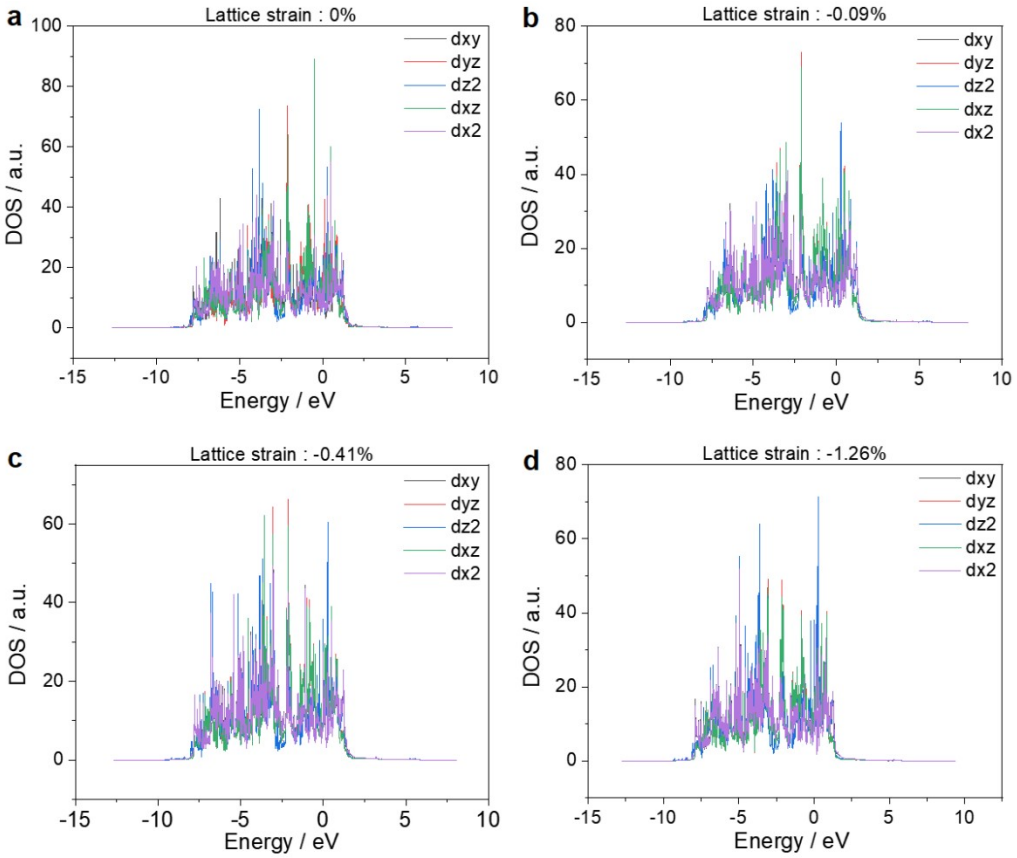


**Figure S19.** Density of states (DOS) of D orbitals for Ir-PFNSs. DOS of D orbitals for Ir-PFNSs with compressive strain of (a) 0, (b) -0.09%, (c) -0.41%, and (d) -1.26%, respectively.

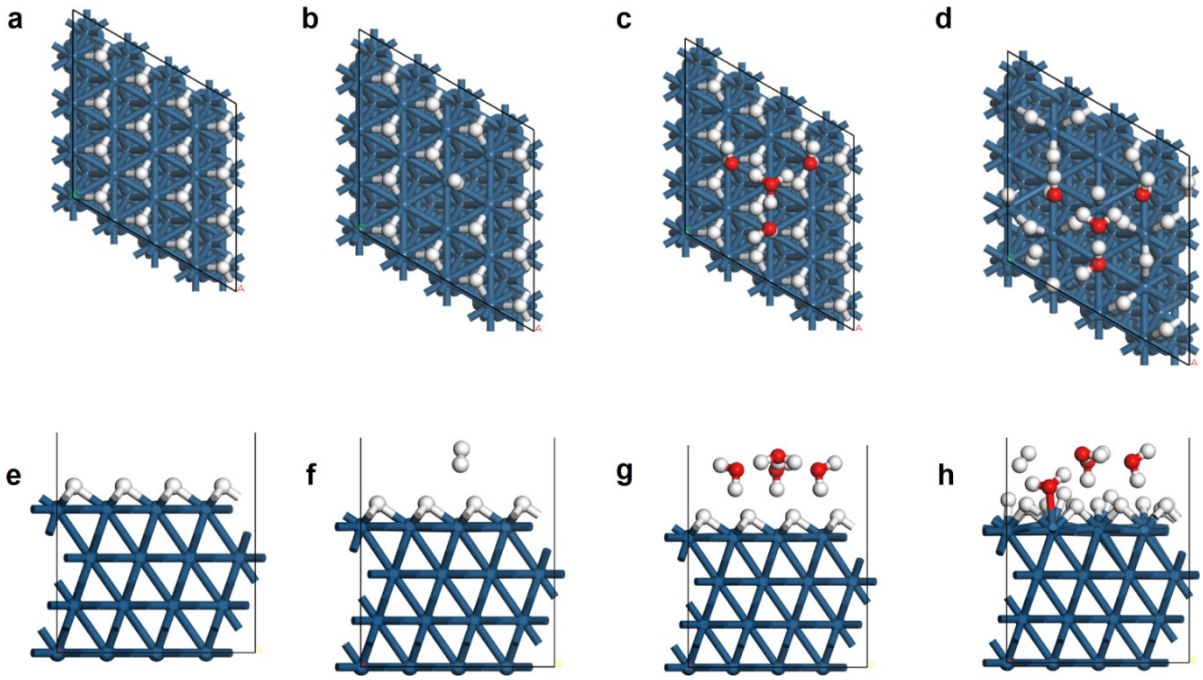


**Figure S20.** The atomic model of Ir-PFNSs for DFT calculations. (a) and (b) are the top views of the initial and final states without $H_3O^+$ participation for Ir-PFNSs with compressive strain of -1.26%, respectively. (c) and (d) are the top views of the initial and final states with $H_3O^+$ participation for Ir-PFNSs with compressive strain of -1.26%, respectively. (e) and (f) are side views of the initial and final states without $H_3O^+$ participation for Ir-PFNSs with compressive strain of -1.26%, respectively. (g) and (h) are the side views of the initial and final states with $H_3O^+$ participation for Ir-PFNSs with compressive strain of -1.26%, respectively. Color code: Iridium, blue; hydrogen, white; oxygen, red.

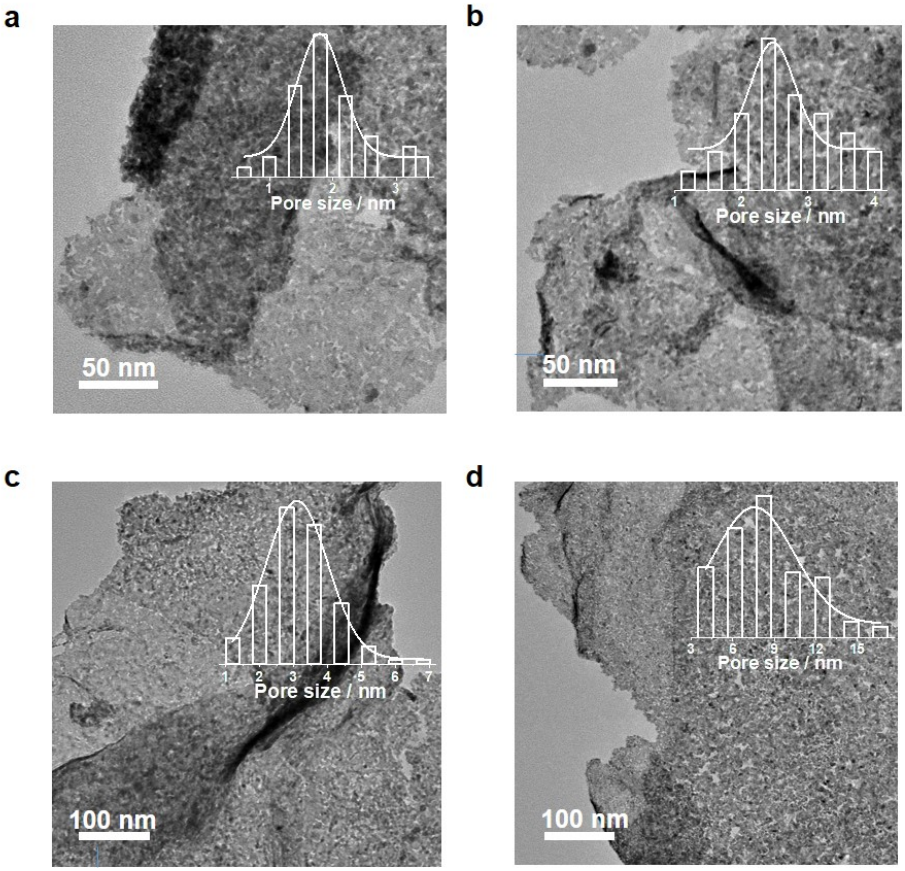


**Figure S21.** The TEM images of Ir-PFNSs with different annealing temperature. (a-d) TEM images of Ir-PFNSs-150, Ir-PFNSs-250, Ir-PFNSs-300 and Ir-PFNSs-400 respectively, where the insets are their histogram of pore size distribution.

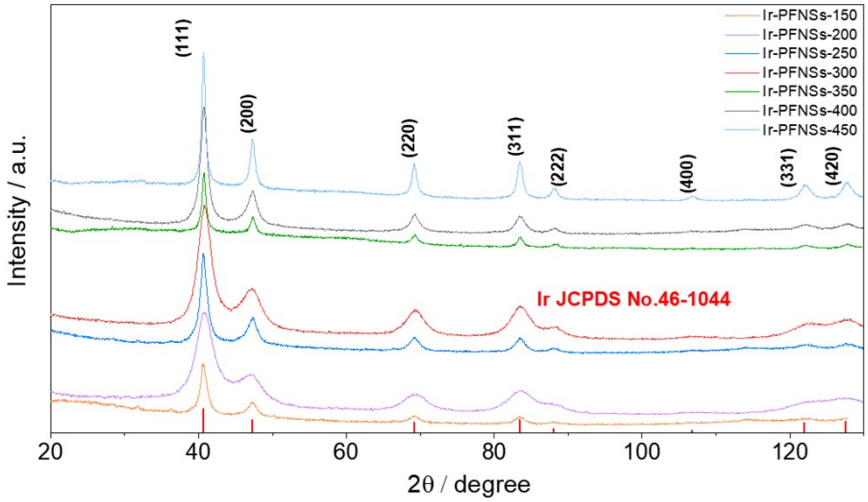


**Figure S22.** XRD patterns of Ir-PFNSs-150, Ir-PFNSs-200, Ir-PFNSs-250, Ir-PFNSs-300 Ir-PFNSs-350, Ir-PFNSs-400 and Ir-PFNSs-450.

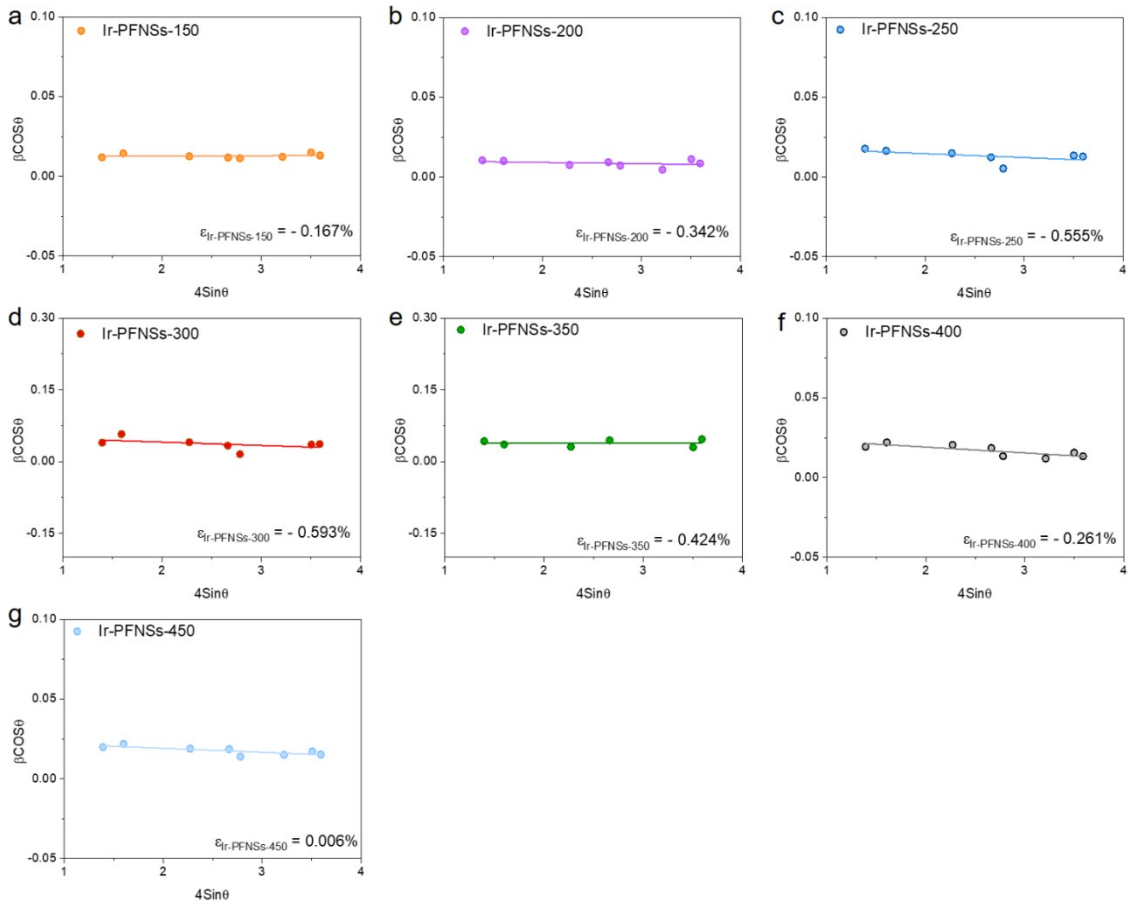


**Figure S23.** The calculation of compressive strain intensity by Williamson-Hall equation. (a) Ir-PFNSs-150, (b) Ir-PFNSs-200, (c) Ir-PFNSs-250, (d) Ir-PFNSs-300, (e) Ir-PFNSs-350, (f) Ir-PFNSs-400 and (g) Ir-PFNSs-450.

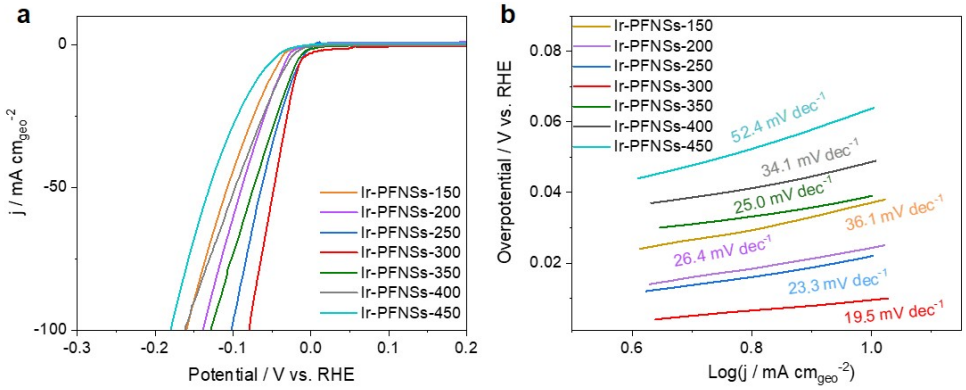


**Figure S24.** HER performance of Ir-PFNSs with different annealing temperatures. (a) HER polarization curves of Ir-PFNSs with different annealing temperature. (b) corresponding Tafel plots obtained from (a).

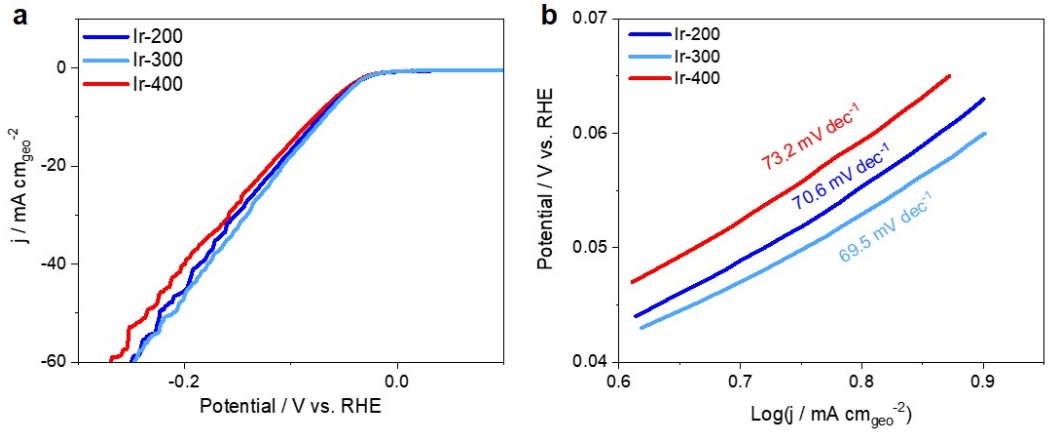


**Figure S25.** HER performance of Ir obtained by annealing Rutile-$IrO_2$ at different annealing temperature in hydrogen atmosphere. (a) HER performances of Ir-200, Ir-300 and Ir-400. (b) corresponding Tafel plots obtained from (a).

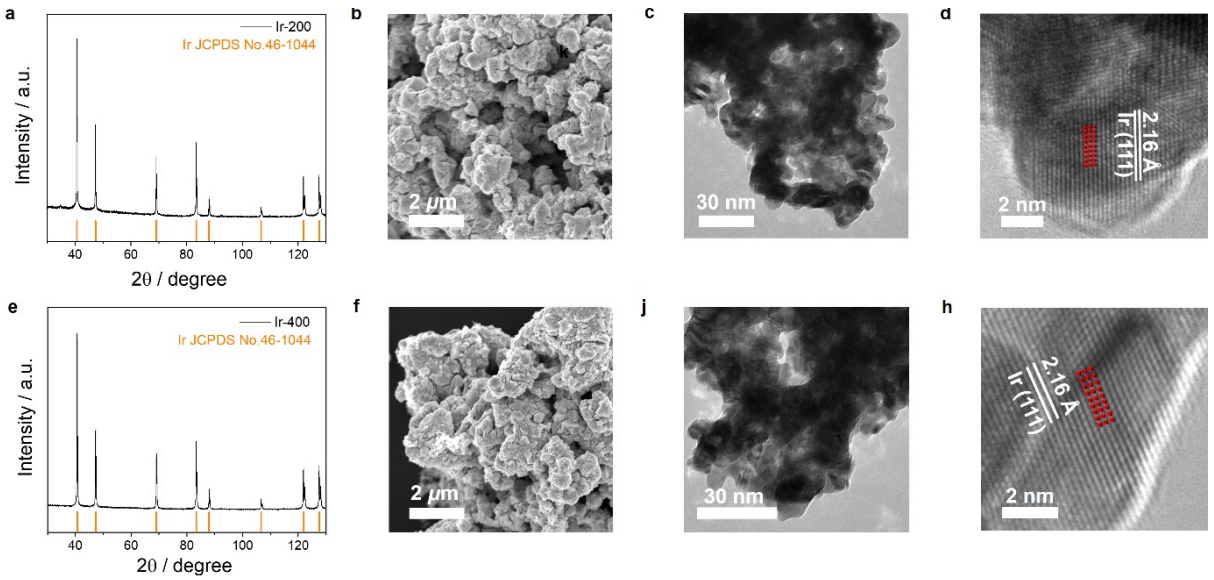


**Figure S26.** XRD patterns, SEM, TEM and HRTEM images of Ir obtained by annealing Rutile-$IrO_2$ at different annealing temperature in hydrogen atmosphere. (a-d) XRD pattern, SEM, TEM and HRTEM images of Ir-200 obtained by annealing Rutile-$IrO_2$ at 200 °C in hydrogen atmosphere. (e-h) XRD pattern, SEM, TEM and HRTEM images of Ir-400 obtained by annealing Rutile-$IrO_2$ at 400 °C in hydrogen atmosphere.

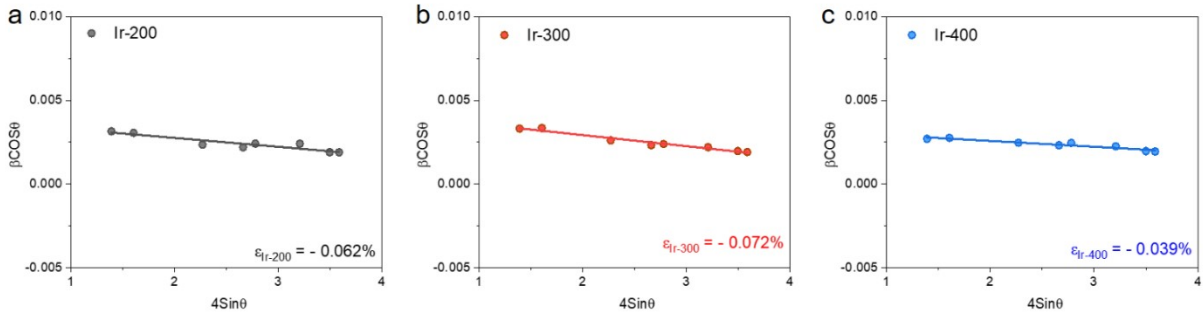


**Figure S27.** The calculation of compressive strain intensity by Williamson-Hall equation. The calculation of compressive strain intensity for (a) Ir-200, (b) Ir-300 and (c) Ir-400.

**Table S1.** Crystallographic information for 3R-$IrO_2$ and Rutile-$IrO_2$.

| Material | Crystal system | Bravais lattice | Unit-cell dimensions | Space group |
|---|---|---|---|---|
| **3R-$IrO_2$** | **Trigonal** | **Primitive** | ***a* = *b* = 3.158 ± 0.006 Å, *c* = 13.617 ± 0.023 Å; *α* = *β* = 90°, *γ* = 120°** | **R-3m (166)** |
| Rutile-$IrO_2$ | Tetragonal | Primitive | $a = b = 4.505$ Å, $c = 3.158$ Å; $\alpha = \beta = \gamma = 90°$ | $P4_2/mnm$ (136) |

**Table S2.** The comparison of HER performance, lattice strain and annealing temperatures for Ir-PFNSs and metallic Ir electrocatalysts.

| Catalysts | Annealing temperature / °C | Lattice strain / % | Overpotential @-10 mV $cm_{geo}^{-2}$ / mV | Tafel slope / mV $dec^{-1}$ |
|---|---|---|---|---|
| **Ir-PFNSs- 150** | 150 | -0.167 | 50 | 36.1 |
| **Ir-PFNSs-200** | 200 | -0.342 | 38 | 26.4 |
| **Ir-PFNSs-250** | 250 | -0.555 | 22 | 23.3 |
| **Ir-PFNSs-300** | 300 | -0.593 | 18 | 19.5 |
| **Ir-PFNSs-350** | 350 | -0.424 | 25 | 25.0 |
| **Ir-PFNSs-400** | 400 | -0.261 | 40 | 34.1 |
| **Ir-PFNSs- 450** | 450 | 0.006 | 65 | 52.4 |
| **Ir-200** | 200 | -0.062 | 72 | 70.6 |
| **Ir-300** | 300 | -0.072 | 69 | 69.5 |
| **Ir-400** | 400 | -0.039 | 76 | 73.2 |

**Table S3.** The comparison of HER activity for the optimal Ir-PFNSs-300 with the previous reported electrocatalysts.

| Catalyst | Substrate | Electrolyte | Catalyst loading / mg $cm^{-2}$ | Overpotential @ 10 mA $cm_{geo}^{-2}$ / mV | Tafel / mV $dec^{-1}$ | Refs |
|---|---|---|---|---|---|---|
| **Ir-PFNSs-300** | GCE | 0.5 M $H_2SO_4$ | 0.056 | 18 | 19.5 | This work |
| **Ir-SA@Fe@NCNT** | GCE | 0.5 M $H_2SO_4$ | 0.285 | 26 | 31.8 | 11 |
| **Co-RuIr** | Au-electrode | 0.1 M $HClO_4$ | 0.051 | 14 | 31.1 | 12 |
| **$Ir_{25}Ni_{33}Ta_{42}$** | Ti holder | 0.5 M $H_2SO_4$ | 0.00814 | 99 | 35 | 13 |
| **NiVIr-LDH** | / | 1.0M KOH | / | 47 | 107 | 14 |
| **PdCu/Ir/C** | GCE | 0.1 M $HClO_4$ | 0.051 | 20 | / | 15 |
| **Ni/np-Ir** | GCE | 0.5 M $H_2SO_4$ | 0.153 | 20 | 26 | 16 |
| **$Ir_{16}$-PdCu/C** | RDE | 0.1 M KOH | 0.00546 | 99 | 90.3 | 17 |
| **$IrMo_{0.59}$ NPs** | GCE | 0.1 M KOH | 0.03 | 38 | 60 | 18 |
| **$IrP_2$@NC** | GCE | 0.5 M $H_2SO_4$ | 0.7 | 8 | 28 | 19 |
| **Ir@N-G-750** | GCE | 0.5 M $H_2SO_4$ | 0.357 | 19 | 26 | 20 |
| **Ir−C≡** | GCE | 1.0 M KOH | 0.04 | 7 | 62 | 21 |
| **$Er_2Si_2O_7$:$IrO_2$** | Carbon Tape | 0.5 M $H_2SO_4$ | / | 76 | 49 | 22 |
| **Ir/SiNW** | GCE | 0.5 M $H_2SO_4$ | 0.339 | 22 | 20 | 23 |
| **IrCo@NC-500** | GCE | 0.5 M $H_2SO_4$ | 0.275 | 24 | 23 | 24 |
| **Ir@CON** | RDE | 0.5 M $H_2SO_4$ | 0.5 | 13.6 | 27 | 25 |
| **$Ir_3V$/C-1000** | RDE | 1.0 M KOH | 0.019 | 9 | 24.1 | 26 |
| **$Mo_2TiC_2Tx$-$Pt_{SA}$** | Carbon paper | 0.05 M $H_2SO_4$ | 1 | 30 | 30 | 27 |

| | | | | | | |
|---|---|---|---|---|---|---|
| **$PtW_6O_{24}$/C** | GCE | 0.5 M $H_2SO_4$ | / | 22 | 29.8 | 28 |
| **Pt-SAs/$WS_2$** | GCE | 0.5 M $H_2SO_4$ | 0.01 | 32 | 28 | 29 |
| **$Pt_1$/OLC** | RDE | 0.5 M $H_2SO_4$ | 0.51 | 38 | 36 | 30 |
| **Pt-SA/ML-$WO_3$** | GC | 0.5 M $H_2SO_4$ | 0.56 | 22 | 27 | 31 |
| **Pt3Co@NCNT** | CFP | 0.5 M $H_2SO_4$ | 0.38 | 42 | 27.2 | 32 |

**Table S4.** The comparison of HER stability for Ir-PFNSs-300 with the previous reported electrocatalysts.

| Catalyst | Test method | Stability | Refs |
|---|---|---|---|
| **Ir-PFNSs-300** | Chronopotentiometry (v-t) | 63 h @10 mA $cm_{geo}^{-2}$ | This work |
| **Co-RuIr** | Chronopotentiometry (v-t) | 25 h @ 10 mA $cm_{geo}^{-2}$ | 12 |
| **$Ir_{25}Ni_{33}Ta_{42}$** | Chronopotentiometry (v-t) | 10 h @ 10 mA $cm_{geo}^{-2}$ | 13 |
| **PdCu/Ir/C** | Chronopotentiometry (v-t) | 10 h @ 20 mA $cm_{geo}^{-2}$ | 15 |
| **Ni/np-Ir** | Chronoamperometry (i-t) | 360 h @ -0.02 $V_{RHE}$ | 16 |
| **$Ir_{16}$-PdCu/C** | Chronoamperometry (i-t) | 10 h @ -0.1 $V_{RHE}$ | 17 |
| **$IrP_2$@NC** | Chronoamperometry (i-t) | 10 h @ -0.02 $V_{RHE}$ | 19 |
| **Ir@N-G-750** | Chronopotentiometry (v-t) | 20 h @ 20 mA $cm_{geo}^{-2}$ | 20 |
| **Ir/SiNW** | Chronopotentiometry (v-t) | 5000 s @ 10 mA $cm_{geo}^{-2}$ | 23 |
| **$Ir_3V$/C-1000** | Chronoamperometry (i-t) | 10000 s @ -0.01 $V_{RHE}$ | 26 |

## References


[1] Z. L. Fan, Y. J. Ji, Q. Shao, S. Z. Geng, W. X. Zhu, Y. Liu, F. Liao, Z. W. Hu, Y. C. Chang, C. W. Pao, Y. Y. Li, Z. H. Kang, M. W. Shao, *Joule* 2021, **5***,* 3221-3234.

[2] V. Wang, N. Xu, J. C. Liu, G. Tang, W. T. Geng, *Comput. Phys. Commun.* 2021, **267**, 108033.

[3] D. Nath, F. Singh, R. Das, *Mater. Chem. Phys.* 2020, 239, 12201.

[4] W. Li, A. M. Lane, *Electrochem. Commun*. 2011, **13**, 913-916.

[5] P. Xiao, M. A. Sk, L. Thia, X. M. Ge, R. J. Lim, J. Y. Wang, K. H. Lim and X. Wang, *Energy Environ*. *Sci*. 2014, **7**, 2624−2629.

[6] J. P. Perdew, K. Burke, M. Ernzerhof, *Phys. Rev. Lett.* 1996, **77**, 3865-3868.

[7] S. Grimme, S. Ehrlich, L. Goerigk, *J. Comput. Chem.* 2011, **32**, 1456-1465.

[8] K. Mathew, V. S. C. Kolluru, S. Mula, S. N. Steinmann, R. G. Hennig, *J. Chem. Phys.* 2014, **140**, 084106.

[9] K. Mathew, R. Sundararaman, K. Letchworth-Weaver, T. A. Arias, R. G. Hennig, *J. Chem. Phys.* 2019, **151**, 234101.

[10] D. A. McQuarrie, Quantum chemistry [M]. *University Science Books*, 2008.

[11] F. Luo, H. Hu, X. Zhao, Z. H. Yang, Q. Zhang, J. X. Xu, T. Kaneko, Y. Yoshida, C. Z. Zhu, W. W. Cai, *Nano Lett*. 2020, **20**, 2120-2128.

[12] J. Q. Shan, T. Ling, K. Davey, Y. Zheng, S. Z. Qiao, *Adv. Mater*. 2019, **31**, 1900510.

[13] Z. J. Wang, M. X. Li, J. H. Yu, X. B. Ge, Y. H. Liu, W. H. Wang, *Adv. Mater*. 2020, **32**, 1906384.

[14] D. W. Wang, Q. Li, C. Han, Q. Q. Lu, Z. C. Xing, X. R. Yang, *Nat. Commun*. 2019, **10**, 3899.

[15] M. G. Li, Z. L. Zhao, Z. H. Xia, M. C. Luo, Q. H. Zhang, Y. N. Qin, L. Tao, K. Yin, Y. G. Chao, L. Gu, W. W. Yang, Y. S. Yu, G. Lu, S. J. Guo, *Angew. Chem. Int. Edit*. 2021, **60**, 8243-8250.

[16] Y. Q. Yu, K. Jiang, M. Luo, Y. Zhao, J. Lan, M. Peng, F. M. F. de Groot, Y. W. Tan, *ACS Nano* 2021, **15**, 5333-5340.

[17] Y. N. Qin, Z. C. Wang, W. H. Yu, Y. J. Sun, D. Wang, J. P. Lai, S. J. Guo, L. Wang, *Nano Lett*. 2021, **21**, 5774-5781.

[18] L. H. Fu, Y. B. Li, N. Yao, F. L. Yang, G. Z. Cheng, W. Luo, *ACS Catal*. 2020, **10**, 7322-7327.

[19] Z. H. Pu, J. H. Zhao, I. S. Amiinu, W. Q. Li, M. Wang, D. P. He, S. C. Mu, *Energ.. Environ. Sci*, 2019, **12**, 952-957.

[20] X. J. Wu, B. M. Feng, W. Li, Y. L. Niu, Y. A. Yu, S. Y. Lu, C. Y. Zhong, P. Y. Liu, Z. Q. Tian, L. Chen, W. H. Hu, C. M. Li, *Nano Energy* 2019, **62**, 117-126.

[21] Y. Peng, Q. M. Liu, B. Z. Lu, T. He, F. Nichols, X. Hu, T. Huang, G. Huang, L. Guzman, Y. Ping, S. W. Chen, *ACS Catal*. 2021, **11**, 1179-1188.

[22] P. Karfa, K. C. Majhi, R. Madhuri, *ACS Catal*. 2018, **8**, 8830-8843.

[23] M. Q. Sheng, B. B. Jiang, B. Wu, F. Liao, X. Fan, H. P. Lin, Y. Y. Li, Y. Lifshitz, S. T. Lee, M. W. Shao, *ACS Nano* 2019, **13**, 2786-2794.

[24] P. Jiang, J. T. Chen, C. L. Wang, K. Yang, S. P. Gong, S. Liu, Z. Y. Lin, M. S. Li, G. L. Xia, Y. Yang, J. W. Su, Q. W. Chen, *Adv. Mater*. 2018, **30**, 1705324.

[25] J. Mahmood, M. A. R. Anjum, S. H. Shin, I. Ahmad, H. J. Noh, S. J. Kim, H. Y. Jeong, J. S. Lee, J. B. Baek, *Adv. Mater*. 2018, **30**, 1805606.

[26] L. W. Chen, X. Guo, R. Y. Shao, Q. Q. Yan, L. L. Zhang, Q. X. Li, H. W. Liang, *Nano Energy* 2021, **81**, 105636.

[27] J. Q. Zhang, Y. F. Zhao, X. Guo, C. Chen, C. L. Dong, R. S. Liu, C. P. Han, Y. D. Li, Y. Gogotsi, G. X. Wang, *Nat. Catal*. **2018**, *1*, 985-992.

[28] F. Y. Yu, Z. L. Lang, L. Y. Yin, K. Feng, Y. J. Xia, H. Q. Tan, H. T. Zhu, J. Zhong, Z. H. Kang, Y. G. Li, *Nat. Commun*. 2020, **11**, 490.

[29] Y. Shi, Z. R. Ma, Y. Y. Xiao, Y. C. Yin, W. M. Huang, Z. C. Huang, Y. Z. Zheng, F. Y. Mu, R. Huang, G. Y. Shi, Y. Y. Sun, X. H. Xia, W. Chen, *Nat. Commun.* 2021, **12**, 3021.

[30] D. B. Li, X. Y. Li, S. M. Chen, H. Yang, C. D. Wang, C. Q. Wu, Y. A. Haleem, S. Duan, J. L. Lu, B. H. Ge, P. M. Ajayan, Y. Luo, J. Jiang, L. Song, *Nat. Energy* 2019, **4**, 512-518.

[31] D. L. Wang, H. P. Li, N. Du, W. G. Hou, *Adv. Funct. Mater*. 2021, **31**, 2009770.

[32] P. Y. Kuang, Y. R. Wang, B. C. Zhu, F. J. Xia, C. W. Tung, J. S. Wu, H. M. Chen, J. G. Yu, *Adv Mater*. 2021, **33**, 2008599.